# Supporting Information

**Tubular Structures from the LnS-$TaS_2$ (Ln=La, Ce, Nd, Ho, Er) and LaSe-$TaSe_2$ Misfit Layered Compounds****

Gal Radovsky, Ronit Popovitz-Biro, Tommy Lorenz, Gotthard Seifert, Jan-Ole Joswig, Lothar Houben, Rafal E. Dunin-Borkowski, Reshef Tenne*

## Table of Contents



## 1. Structural aspects of the nanotubes determined from electron diffraction patterns

### 1.1 Rotational variants

In many cases, rotational variants of both the LnS and the $TaS_2$ subsystems of the nanotubes about their common *c*-axis were observed, just as in their PbS-$NbS_2$[14] and PbS-$TaS_2$[7] counterparts. The observation of rotational variants of the LnS layers results from the fact that there are three equivalent *b* directions (labeled according to the ortho-pseudohexagonal system) in $TaS_2$, as marked by green arrows in Figures 1b and S1. The *b*-axis of the LnS layer can therefore be superimposed on $TaS_2$ in three rotational variants, which are rotated azimuthally by 60° about their common *c*-axis, as shown in Figure S1.[7,13,16-18,S1] With regard to the rotational variants of the $TaS_2$ layers, since the difference between the *a* and the *b* lattice parameters of the modulated LnS (or PbS, SnS) is small (below 1.5% for SnS, PbS, LaS, NdS

and larger for HoS and ErS), the *b*-axis of $TaS_2$ can be superimposed onto either the *b*-axis or the *a*-axis of LnS, which differ by 90°, as shown in Figure S1.

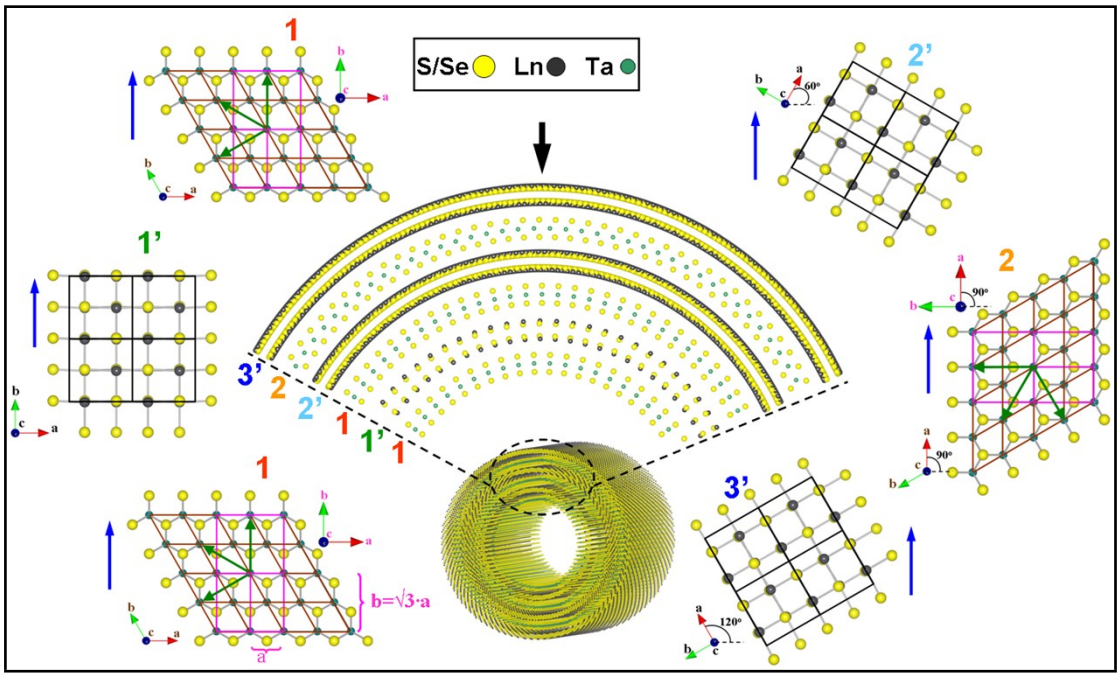


Figure S1. (reproduced from reference [18]). Schematic diagram showing the possible stacking of the LnS and $TaS_2$ layers along their common *c*-axis and their in-plane orientations for tubules containing rotational variants of the LnS and $TaS_2$ layers. Two types of $TaS_2$ layers are denoted "1" and "2". Three types of LnS layers are denoted "1' ", "2' " and "3' ". For each layer, a head-on view along the *c*-axis is shown (assuming a flat layer in the area marked by the black arrow). The tubule axis is marked by blue arrows. For the $TaS_2$ layers, pseudohexagonal and ortho-pseudohexagonal unit cells are shown in brown and purple, respectively. The relationship between the two unit cells is shown at the bottom left for the head-on view of the $TaS_2$ type "1" layer. Three equivalent "*b*" directions are indicated by green arrows, according to the ortho-pseudohexagonal unit system, in each of the $TaS_2$ projections.

### 1.2 Chirality of the nanotubes

Helical folding of the $TaS_2$(Se) and LnS(Se) layers results in differences in lattice orientation between the upper and lower walls of the tubule. As a result, diffraction spots corresponding to in-plane reflections (i.e., 10.0, 11.0 of $TaS_2$(Se) and 200, 020, 110, 220 of LnS(Se)) are split within an azimuthal angle that is twice the chiral angle.

## 2. Chemical analysis of the products

Representative examples of EDS analysis of the individual LnS-$TaS_2$ tubes within the TEM are shown in Figure S2. A spectrum recorded from a LaSe-$TaSe_2$ tubule produced by the addition of $TaBr_5$ powder to the ampoule is also shown. Chlorine peaks are clearly visible in the EDS spectra of LnS-$TaS_2$ with (Ln=La,Ce,Nd) (Figures S2a-c) and LnSe-$TaSe_2$ (Figure S2f) MLC nanotubes. However, no clear Cl peak could be detected for Ln=Ho and Er MLC nanotubes. (Figures S2d-e) Also, a Br peak was clearly visible in EDS spectra recorded from LaSe-$TaSe_2$ nanotubes when $TaBr_5$ was added (Figure S2g). EDS analysis of LnS-$TaS_2$ nanotubes with (Ln=La,Ce, Nd) and LaSe-$TaSe_2$ indicated the presence of 1-2 at% Cl. Same amount of Br was found for LaSe-$TaSe_2$ nanotubes when $TaBr_5$ was added.

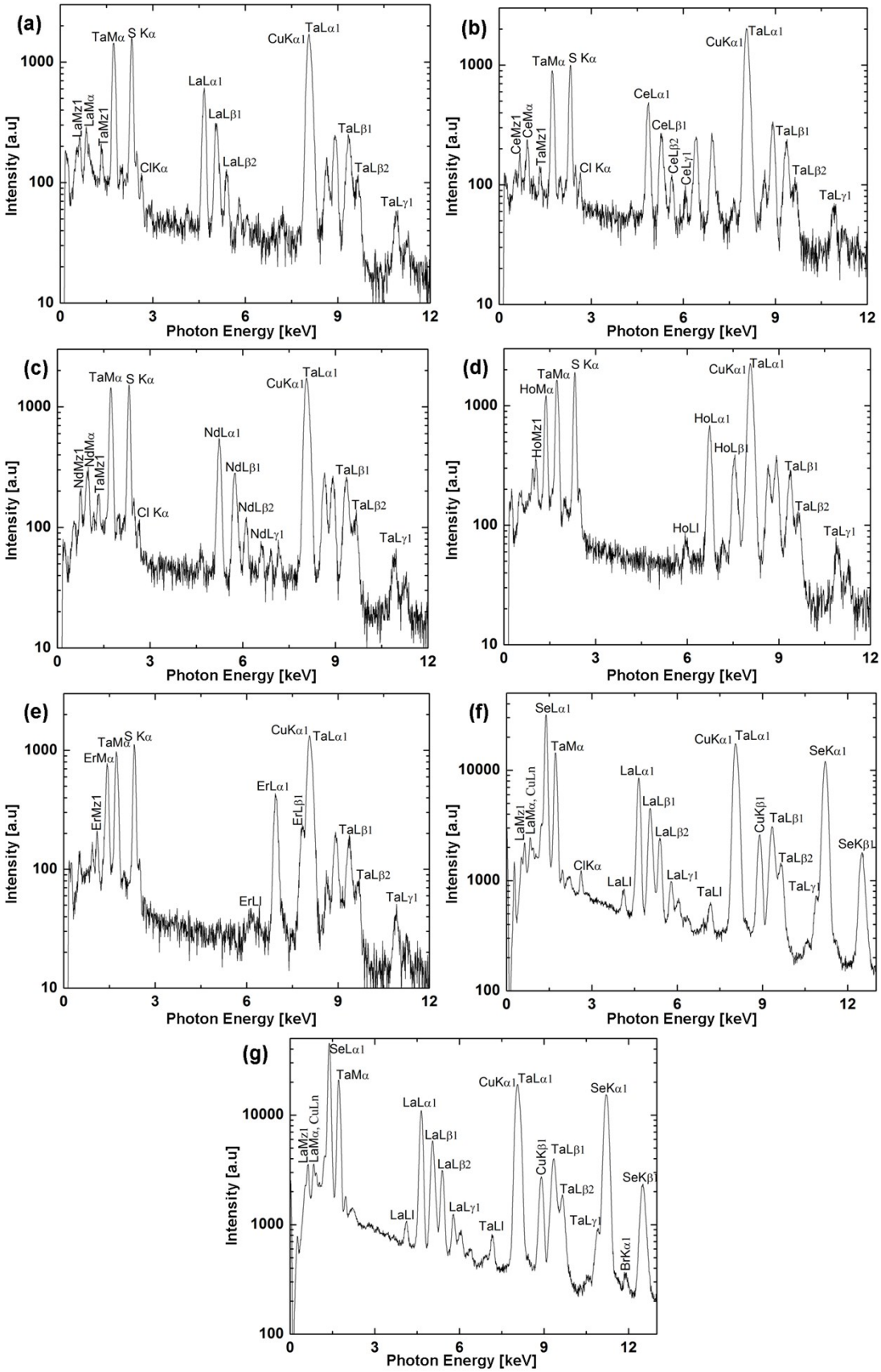


Figure S2. Representative EDS spectra recorded from LnS-$TaS_2$ tubular structures, for which LnS is: (a) LaS, (b) CeS, (c) NdS, (d) HoS and (e) ErS. The (unmarked) peaks appearing at 8.65 keV and 8.92 keV in (a)-(e) are $ZnK_{\alpha 1}$ and $CuK_{\beta 1}$, originate from the TEM grid. The peaks at 6.42 keV and 6.93 keV in (b) are $FeK_{\alpha 1}$ and $CoK_{\alpha 1}$, respectively. They are attributed to the mechanical aperture in the TEM column. (f) and (g) are representative

spectra recorded from LaSe-$TaSe_2$ tubular structures synthesized by the catalytic action of $TaCl_5$ and $TaBr_5$, respectively.

# 3. SEM images of the product.

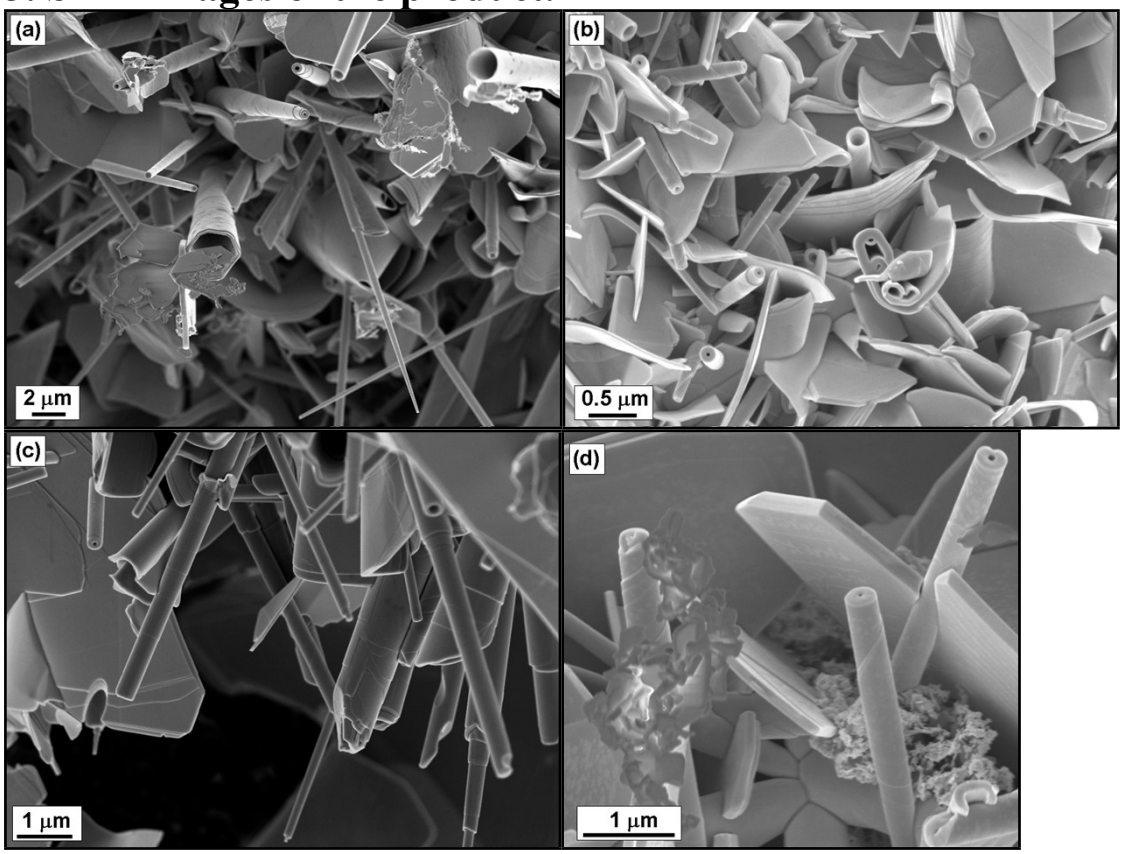


Figure S3. SEM images of the tubular structures and common by-products from (a) NdS-$TaS_2$, (b) HoS-$TaS_2$, (c) CeS-$TaS_2$ and (d) LaSe-$TaSe_2$ MLC. Scrolling steps are visible at the significant part of the tubular crystals.

## 4. X-Ray diffraction analysis of the product

Figure S4 show the XRD patterns of the total products obtained during the attempts to synthesize NdS-$TaS_2$ (a) and ErS-$TaS_2$ (b) MLC tubules. The MLC nanotubes' yield in these cases was 20%.

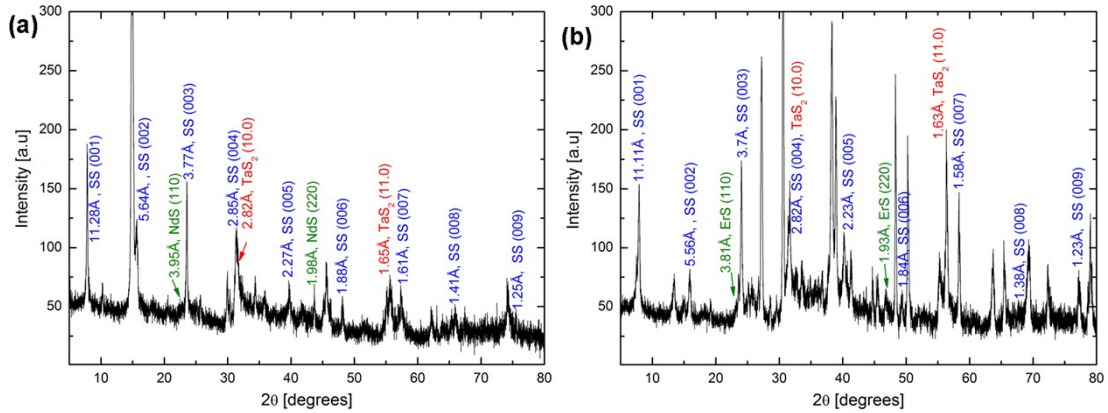


Figure S4. Representative XRD patterns recorded from the total products obtained during the synthesis of (a) NdS-$TaS_2$ and (b) ErS-$TaS_2$ tubular structures. Different orders of peaks associated with the LnS/$TaS_2$ (1:1) superstructure (SS) along the common *c*-axis are marked in blue. The corresponding interplanar spacings are also marked.

## 5. Tubular structures from LnS-$TaS_2$ (Ln=Ce, Nd, Ho) and LaSe-$TaSe_2$ MLC with a single folding vector of LnS(Se) and $TaS_2$(Se)

As was mentioned in the main text, the in-plane lattice parameters *a* and *b* of LnS(Se) and $TaS_2$(Se) (labeled according to the ortho-pseudohexagonal system) were calculated from the (10.0) and (11.0) reflections of $TaS_2$ and the (220) reflections of LnS and are summarized in Table 2. The *b*-axis is commensurate and common to both the LnS and the $TaS_2$ and was assumed to be equal for the calculations.

**5.1 Tubular structures from LaSe-$TaSe_2$ MLC with a single folding vector of LnSe and $TaSe_2$**

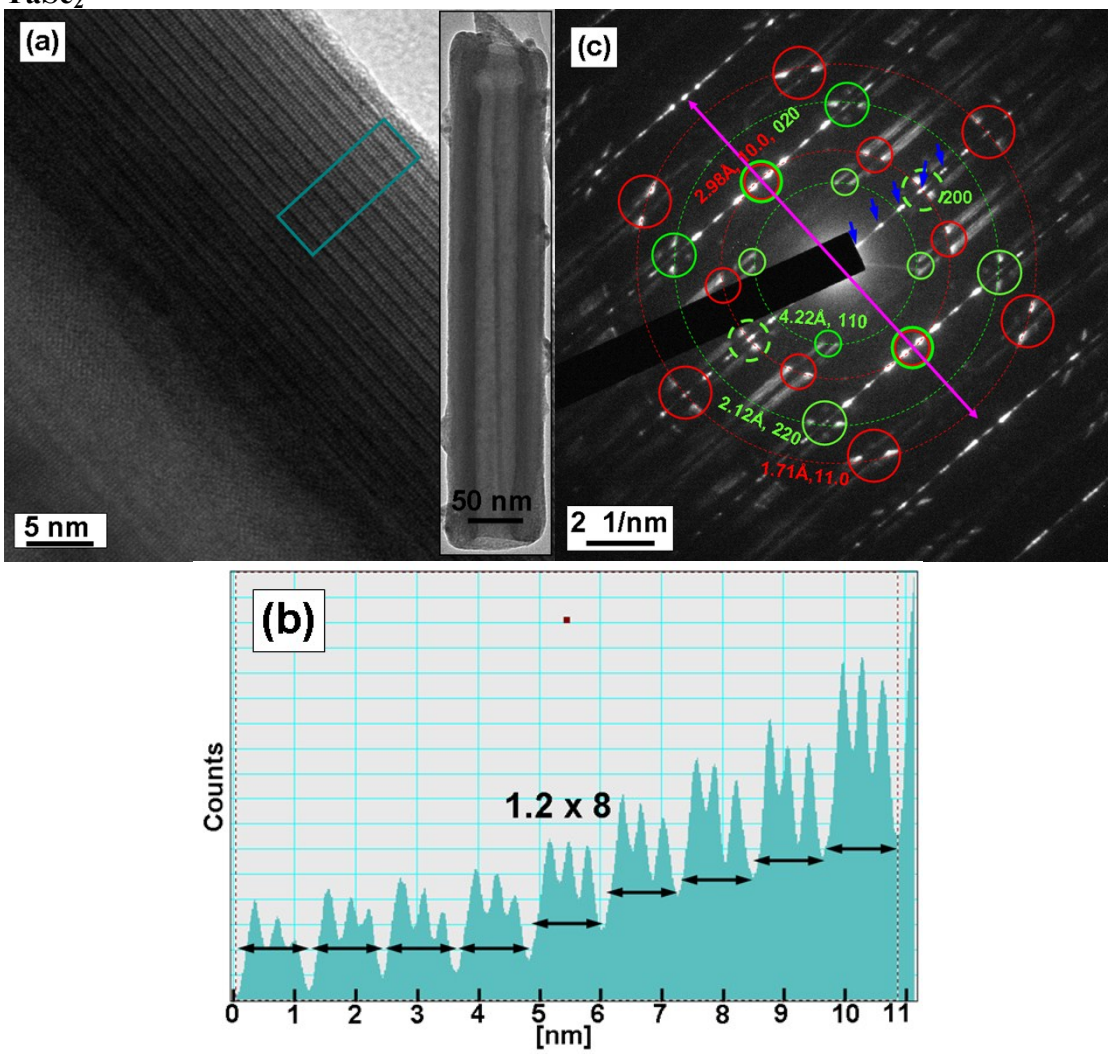


Figure S5. TEM images of LaSe-$TaSe_2$ tubular crystal, with the LaSe and $TaSe_2$ layers stacked periodically. (a) High magnification image with low magnification image shown as inset. (b) Line profiles integrated along the rectangle marked in (a). (c) SAED pattern acquired from the area shown in (a). Spots corresponding to the same interplanar spacings are marked by large segmented ellipses or circles (red for $TaSe_2$ and green for LaSe) and the respective Miller indices are indicated. The tubule axis is marked by purple double arrow. Basal reflections are marked by small blue arrows. Chiral angles of 5.4° for both the $TaSe_2$ and LnSe layers were determined from the splitting of the spots, as discussed in the text.

## 5.2. Tubular structures from NdS-$TaS_2$ and HoS-$TaS_2$ MLC with a single folding vector of LnS and $TaS_2$

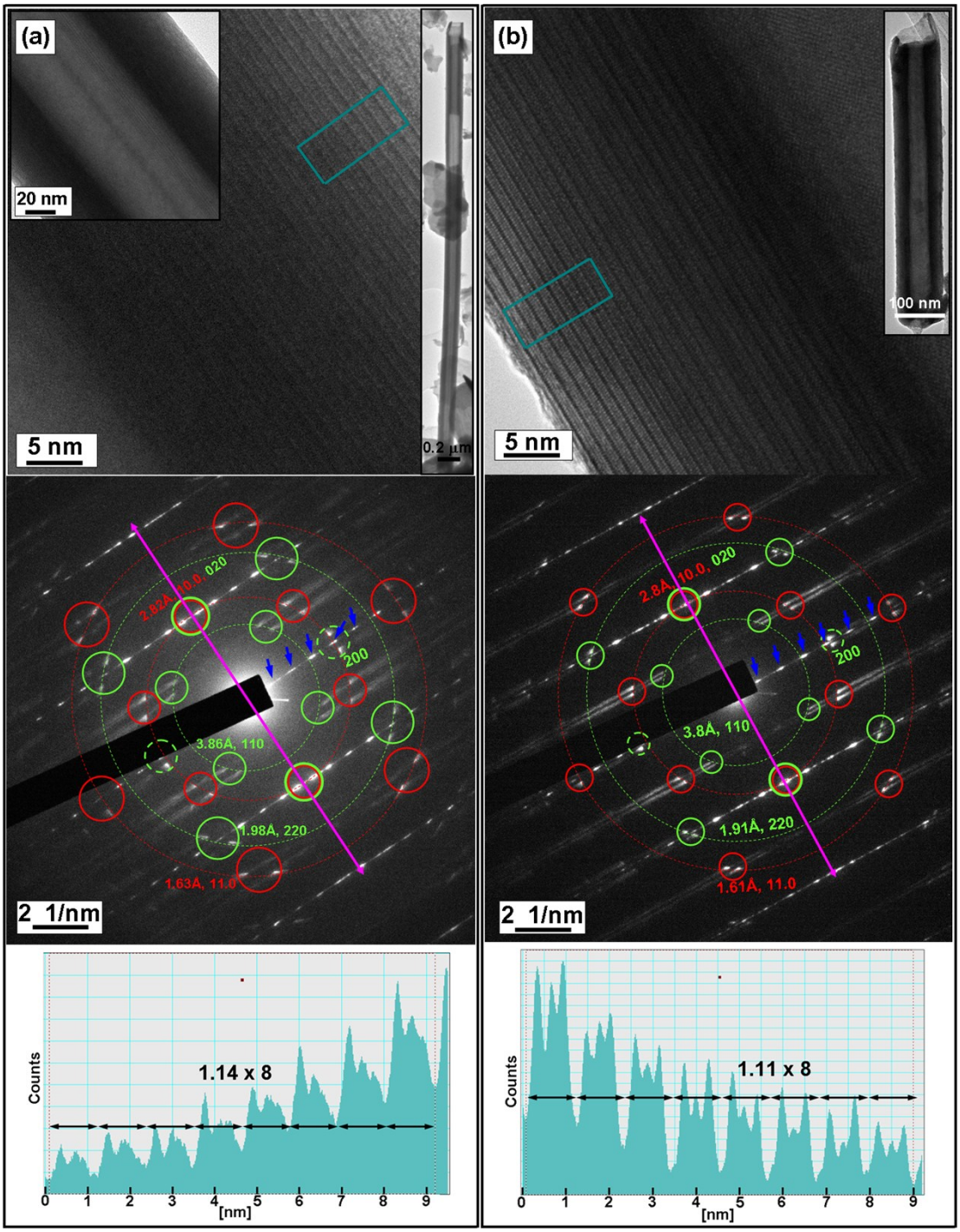


Figure S6. TEM images of (a) NdS-$TaS_2$ and (b) HoS-$TaS_2$ nanotubes, with the LnS and $TaS_2$ layers stacked periodically. Top: High magnification images, with low and medium magnification images shown as insets. Middle: SAED patterns recorded from the areas shown in the upper images. Spots corresponding to the same interplanar spacings are marked by large segmented circles (red for $TaS_2$ and green for LnS) and the respective Miller indices are indicated. The tubule axes are marked by purple double arrows. Basal reflections are marked by small arrows. Chiral angles of 6° and 2.5° for the tubules shown in (a) and (b), respectively, were determined from the splitting of the spots, as discussed in the text. Bottom: Line profiles integrated along the rectangles marked in the upper images.

## 5.3. Tubular structures from the Ce-Ta-S compound

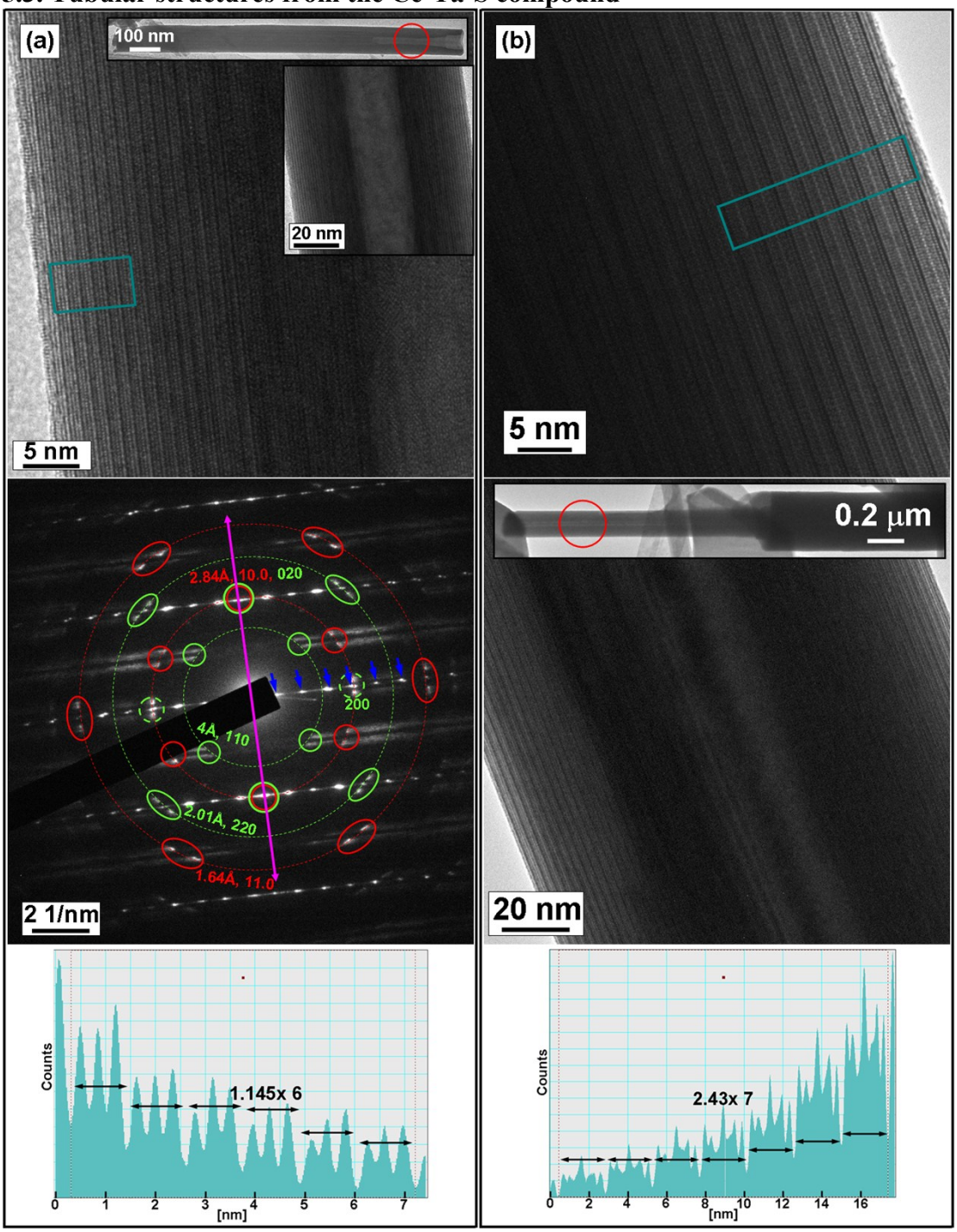


Figure S7. TEM images of CeS-$TaS_2$ tubular crystals. (a) LnS and $TaS_2$ layers stacked periodically according to the (1:1) superstructure. Top: High, medium and low (insets) magnification images. (The high magnification image was taken from the area marked by the red circle in the inset). Middle: SAED pattern taken from the area shown in the upper image. Spots corresponding to the same interplanar spacing are marked by the large segmented circles (red $TaS_2$, green LnS) and Miller indices are indicated. Tubule axis is marked by the purple double arrow. Basal reflections are marked by the blue small arrows. The chiral angle ($4^o$) for the tubule shown in (a) was determined from the splitting of the spots as discussed in the text. Bottom: Line profile integrated along the rectangle marked in the upper image. (b) Ce-Ta-S tubule with a complex stacking of the layers with 2.43 nm

periodicity along the *c*-axis. (In both (a) and (b), the high magnification image was taken from the area marked by the red circle in the inset).

## 5.4. Tubular structures with a stacking disorder

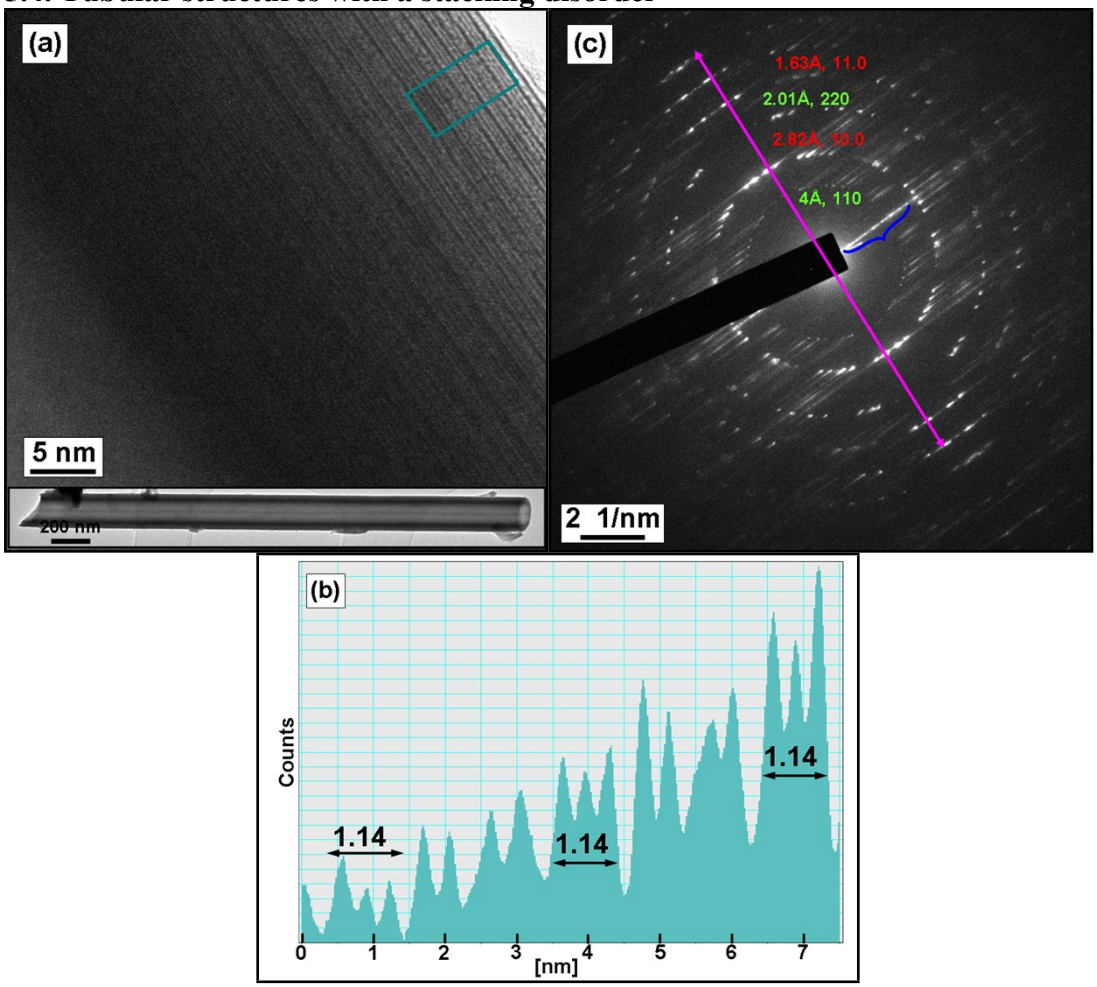


Figure S8. (a) High magnification and (inset) low magnification TEM images of a NdS-$TaS_2$ nanotube with disordered stacking of the LnS and $TaS_2$ layers along the *c*-axis. (b) Line profile integrated along the rectangle marked in (a). (c) SAED pattern recorded from the area shown in (a). Spots corresponding to the same interplanar spacings are distributed on ring-like patterns. Their interplanar spacings and Miller indices are indicated (red for $TaS_2$ and green for NdS). The tubule axis is marked by a purple double arrow.

## 6. Literature values of interplanar spacings of $TaS_2$(Se) and LnS(Se)

| Compound | d (11.0)=d(200)* =a/2 [Å] | d (10.0)=d(020)* =b/2 [Å] | Space group | ICSD col. Code/Reference |
|---|---|---|---|---|
| Pristine bulk 2H-$TaS_2$ | 1.66 | 2.87 | *P63/mmc* | 68488 |
| Pristine bulk 2H-$TaSe_2$ | 1.72 | 2.97 | *P63/mmc* | 18130 |
| $TaS_2$ within $(LaS)_{1.13}TaS_2$ MLC | 1.65 | 2.89 | *Fm2m* | 69582 |
| $TaS_2$ within $(CeS)_{1.15}TaS_2$ MLC | 1.65 | 2.88 | *Fm2m* | 69584 |
| $TaS_2$ within $(NdS)_{1.17}TaS_2$ MLC | 1.66 | 2.86 | | Ref. [10] |
| $TaS_2$ within $(ErS)_{1.23}TaS_2$ MLC | 1.66 | 2.82 | | Ref. [10] |

| Compound | d(200)=a/2 | d(020)=b/2 | d(220) | d(110) | Space group | ICSD col. Code/Reference |
|---|---|---|---|---|---|---|
| LaS within $(LnS)_{1.13}TaS_2$ MLC | 2.91 | 2.89 | 2.05 | 4.1 | *Cm2a* | 69581 |
| Pristine bulk LaS | 2.92 | 2.92 | 2.07 | 4.13 | *Fm-3m* | 641816 |
| CeS within $(CeS)_{1.15}TaS_2$ MLC | 2.87 | 2.875 | 2.03 | 4.06 | *Cm2a* | 69583 |
| Pristine bulk CeS | 2.89 | 2.89 | 2.04 | 4.08 | *Fm-3m* | 603041 |
| NdS within $(NdS)_{1.17}TaS_2$ MLC | 2.84 | 2.86 | | | | Ref. [10] |
| Pristine bulk NdS | 2.85 | 2.85 | 2.01 | 4.03 | *Fm-3m* | 76603 |
| Pristine Bulk HoS | 2.73 | 2.73 | 1.93 | 3.86 | *Fm-3m* | 639661 |
| ErS within $(ErS)_{1.23}TaS_2$ MLC | 2.69 | 2.82 | | | | Ref. [10] |
| Pristine bulk ErS | 2.7 | 2.7 | 1.91 | 3.82 | *Fm-3m* | 53414 |
| Pristine bulk LaSe | 3.03 | 3.03 | 2.145 | 4.29 | *Fm-3m* | 941926 |

Table S1. Literature values of the interplanar spacings of $TaS_2$(Se) and LnS(Se).
* The (11.0) and (10.0) planes, according to the pseudohexagonal system of labeling for $TaS_2$(Se), are equivalent to the (200) and (020) planes, respectively, according to the ortho-pseudohexagonal system.

## 7. Theoretical calculations

### 7.1 Computational details

Calculations were based on the density-functional tight-binding (DFTB) method. Rectangular periodic boundary conditions were applied. The effective one-electron potential in the Kohn−Sham Hamiltonian is approximated as a superposition of the potentials of the neutral atoms. Moreover, only one- and two-center integrals are calculated to set-up a scalar relativistic Hamilton matrix. Hence, relativistic effects are incorporated in a scalar relativistic way. The

valence basis, including the 6s, 6p, and 5d orbitals for La, the 3s and 3p orbitals for S and the 5s, 5p, and 4d orbitals for Ta were used. States below these levels were treated within a frozen-core approximation.

The total and partial densities of states were calculated for rectangular supercells with edge-lengths of 23.2 Å and 11.6 Å in the in-plane directions and 23 Å in the direction perpendicular to the layer. Thus the cells contained 64 LaS and 56 $TaS_2$ formula units. For the DFTB calculations a set of 15 special k-points according to Monkhorst and Pack[S2] were used. Large-diameter multiwall nanotubes were approximated by flat bulk phases and monolayers of the misfit compound and its sublattices. In this way and by the use of periodic boundary conditions in all three dimensions, it was possible to reduce the computational effort significantly. This approximation is considered to be reasonable, as nanotubes with large diameters have very small curvatures. It has been used successfully in many previous studies of curved nanostructures.[S3–S6] The atomic charges were calculated out of a Mulliken population analysis.
The structure that was used for the present calculations contained 4 unit cells of LaS and 7 unit cells of $TaS_2$ in the *a* direction. The different values result from the mismatch between the LaS and $TaS_2$ lattice constants. This choice leads to a structure that has been published by Fang et. al.[23] As reported previously[23,S7-S15] the supercell of this misfit compound consists of two LaS and two $TaS_2$ layers. The $TaS_2$ sublattice has a so-called F-centered and the LaS sublattice a C-centered structure (see Figure 4 in Reference [S7]). Figure S9 shows that the electronic structures obtained by the DFTB method are comparable to the full density functional theory (DFT) method. Therefore the use of the DFTB method for the calculations is justified.

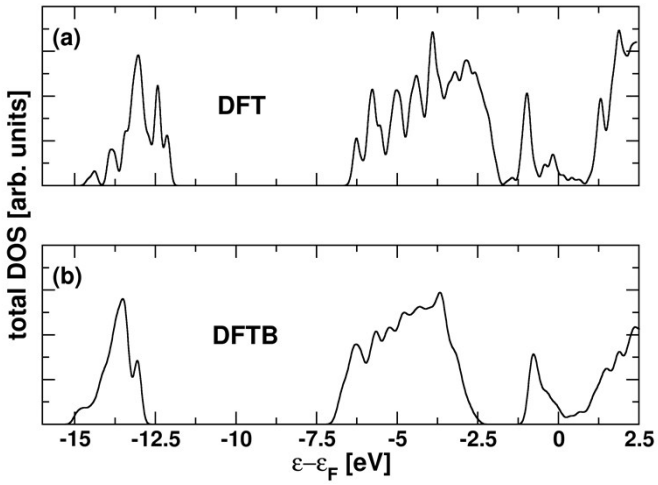


Figure S9. Total density of states for the LaS-$TaS_2$ compound calculated by (a) DFT and (b) DFTB methods.

### 7.2 Calculated density of states of the isolated LaS and $TaS_2$ sublayers

The calculated density of states (DOS) of the isolated LaS and $TaS_2$ sublayers are shown in Figure S10. From these diagrams, it is evident that the *d* states of La and Ta dominate the DOS near the respective Fermi energies. Furthermore, the Fermi energy of $TaS_2$ is slightly below that of LaS. For this reason, as well as due to the fact that both isolated subsystems show metallic behavior, electron transfer from La to Ta in the combined system may be assumed.

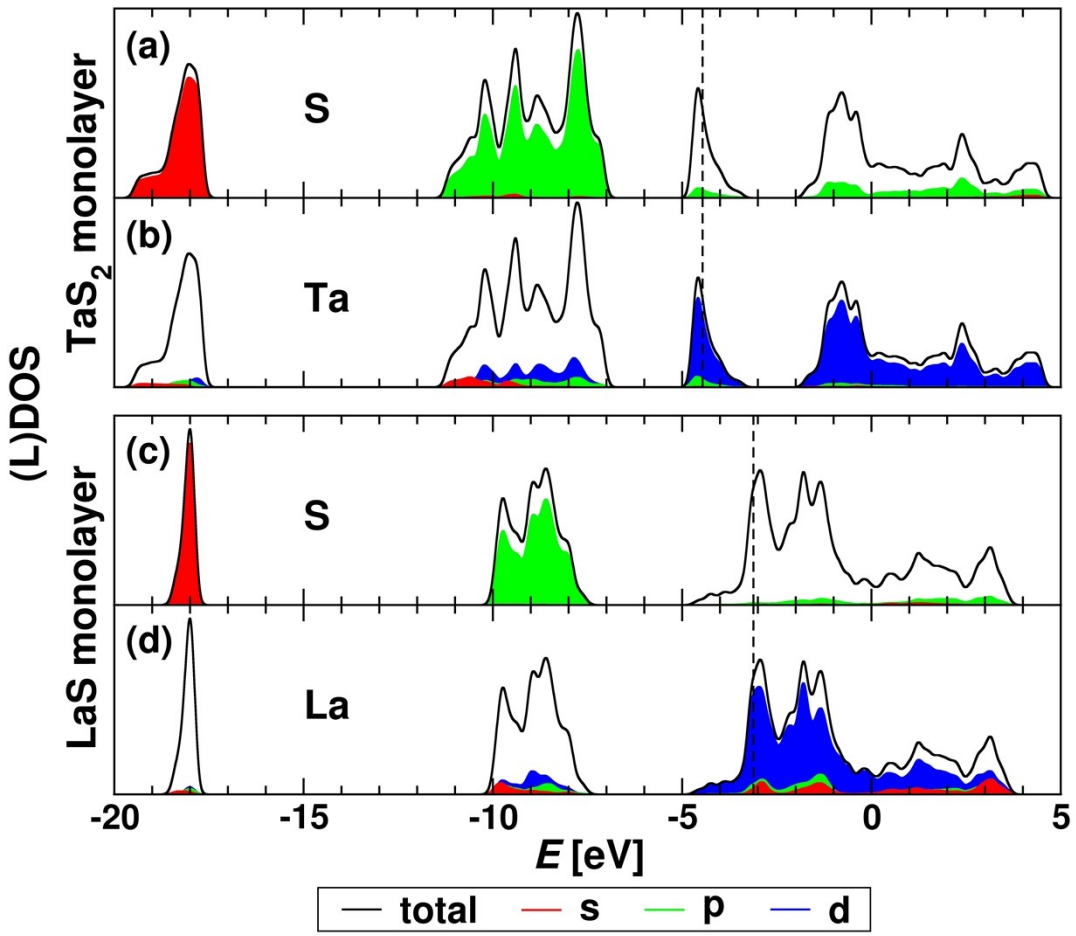


Figure S10. Density of states (DOS) calculated for isolated LaS and $TaS_2$ monolayers. (a) shows the local density of states (LDOS) of all S atoms in the $TaS_2$ monolayer, (b) the LDOS of the Ta atoms in the same layer, (c) the LDOS of the S atoms in the LaS monolayer and (d) the LDOS for the La atoms in this layer. In each diagram, the Fermi energy is displayed as a dashed black line and the total DOS of the monolayer is represented by the black curve. For all atoms, the individual projected orbitals are drawn as colored areas: red for *s*, green for *p* and blue for *d* states. The energy is given relative to "vacuum zero".

### 7.3 Averaged values of the changes in the atomic charges of the atoms in the $(LaS)_{1.14}TaS_2$ MLC

| | | **$\Delta Q$ (ML) [e]** | **$Q$ (sublayer) in LaS-$TaS_2$** |
|---|---|---|---|
| **$TaS_2$ in LaS-$TaS_2$** | Ta | –0.69 | –0.24 [e/$TaS_2$]* |
| | S | +0.23 | |
| **LaS in LaS-$TaS_2$** | La | +0.28 | +0.21 [e/LaS]* |
| | S | –0.07 | |

Table S2. Charge balance of the atoms in the LaS-$TaS_2$ compound. $\Delta Q$ (ML) represents the change of charge for the individual atom type (averaging over all the atoms of this type) in the misfit compound with respect to its charge in an isolated monolayer. $Q$ (sublayer) is the charge of the sublayer in the combined system. The numbers were calculated out of a Mulliken population analysis. *The ratio between 0.24 and 0.21 is in accordance with the exact stoichiomentry of $(LaS)_{1.14}TaS_2$.

## 8. References (SI)


(S1) A. R. Landa-Canovas, A. Gomez-Herrero and L. C. Otero-Diaz, *Micron*, 2001, **32**, 481-495.

(S2) H. J. Monkhorst and J. D. Pack, *Phys. Rev. B*, 1976, **13**, 5188–5192.

(S3) E. Kalfon-Cohen, O. Goldbart, R. Schreiber, S. R. Cohen, D. Barlam, T. Lorenz, A. Enyashin and G. Seifert, *J. Vac. Sci. Technol. B Microelectron. Nanom. Struct.*, 2011, **29**, 021009(1-8).

(S4) E. Kalfon-Cohen, O. Goldbart, R. Schreiber, S. R. Cohen, D. Barlam, T. Lorenz, J.-O. Joswig and G. Seifert, *Appl. Phys. Lett.*, 2011, **98**, 081908(1-3).

(S5) T. Lorenz, J.-O. Joswig and G. Seifert, *Semicond. Sci. Technol.*, 2014, **29**, 064006(1-6).

(S6) T. Lorenz, D. Teich, J.-O. Joswig and G. Seifert, *J. Phys. Chem. C*, 2012, **116**, 11714–11721.

(S7) T. Lorenz, J.-O. Joswig and G.Seifert, *Beilstein J. Nanotechnol.*, 2014, **5**, 2171–2178.

(S8) A. Jobst and S. van Smaalen, *Acta Cryst.*, 2002, **B58**, 179–190.

(S9) S. van Smaalen, *Mater. Sci.*, 1991, **3**, 1247–1263.

(S10) G. A. Wiegers and R. J. Haange, *Mater. Sci.*, 1990, **2**, 455–463.

(S11) G. A. Wiegers, A. Meetsma, S. van Smaalen, R. Haange, J. Wulff, T. Zeinstra, J. de Boer, S. Kuypers, G. van Tendeloo, J. van Landuyt, S. Amelinckx, A. Meerschaut, P. Rabu and J. Rouxel, *Solid State Commun*. 1989, **70**, 409–413.

(S12) G. A. Wiegers and A. Meerschaut, *Mater. Sci. Forum*, 1992, **100-101**, 101–172.

(S13) G. A. Wiegers, A. Meetsma, R. J. Haange, S. van Smaalen, J. L. de Boer, A. Meerschaut, P. Rabu and J. Rouxel, *Acta Cryst.*, 1990, **B46**, 324–332.

(S14) J. Rouxel, A. Meerschaut and G. A. Wiegers, *J. Alloys Compd.*, 1995, **229**, 144–157.

(S15) Y. Ohno, *Solid State Commun.*, 1991, **79**, 1081–1084.